Damage detection in 3D printed plates using ultrasonic wave propagation supported with weighted root mean square calculation and wavefield curvature imaging

Journal of Physics: Conference Series **2647** (2024) 182003 doi:10.1088/1742-6596/2647/18/182003

Damage detection in 3D printed plates using ultrasonic wave propagation supported with weighted root mean square calculation and wavefield curvature imaging

E Wojtczak[1,2], **M Rucka**[1] **and A Andrzejewska**[1]

[1] Department of Mechanics of Materials and Structures, Faculty of Civil and Environmental Engineering, Gdańsk University of Technology, Narutowicza 11/12, 80-233, Gdańsk, Poland
[2] Author to whom any correspondence should be addressed.

erwin.wojtczak@pg.edu.pl

Abstract. 3D printing (additive manufacturing, AM) is a promising approach to producing light and strong structures with many successful applications, e.g., in dentistry and orthopaedics. Many types of filaments differing in mechanical properties can be used to produce 3D printed structures, including polymers, metals or ceramics. Due to the simplicity of the manufacturing process, biodegradable polymers are widely used, e.g., polylactide (polylactide – PLA) with a practical application for manufacturing complex-shaped elements. The current work dealt with the application of ultrasonic guided waves for non-destructive damage detection and imaging in AM plates. Two specimens with defects were manufactured from PLA filament. Different sizes of damage areas were considered. The specimens were tested using the guided wave propagation technique. The waves were excited using a PZT actuator and recorded contactless with the scanning laser Doppler vibrometry (SLDV) in a set of points located at one surface of the sample. The collected signals were processed with two methods. The first was the weighted root mean square (WRMS) algorithm. Different values of the calculation parameters, namely, averaging time and weighting factor were considered. The WRMS damage maps for both samples were prepared to differentiate between intact and damaged areas. The second approach was wavefield curvature imaging (WCI) which allowed the determination of damage maps based on the curvature of the wavefront. The compensation of wave signals was performed to enhance the quality of results. It was observed that the size of the defect strongly influenced the efficiency of imaging with both methods. The limitations of the proposed approaches were characterized. The presented results confirmed that guided waves are promising for non-destructive damage imaging in AM elements.

1. Introduction

Additive manufacturing (AM), also known as 3D printing is currently becoming a promising approach with a great interest in many branches of industry, including dentistry and jaw surgery [1–4] or orthopedics [5–9]. There are many types of AM materials that can be used for the production of 3D printed elements, including biodegradable polymers, which are common due to the simplicity of the manufacturing process and the lack of need for advanced equipment. One of the common filaments is polylactide (polylactic acid – PLA). Polylactide is a biodegradable thermoplastic polyester made from fermented plant starch from corn, cassava, maize, sugarcane or sugar beet pulp. Its melting temperature ranges between 160 and 180°C, while its glass transition temperature ranges between 50

and 60°C. This makes PLA a relatively well-available, eco-friendly material that is easy to process with additive manufacturing technologies [10–12]. The specificity of the AM production process is associated with some challenging problems. The first important issue is that material discontinuities or inhomogeneities may occur in the manufactured elements, such as voids (absence of filament) or areas of uneven filament distribution resulting in local changes in material density. These damage types of damage can occur in the internal structure of the samples, thus they cannot be detected by visual inspecion. The other problem is that AM elements are sensitive to the potentially destructive effects of high fabrication temperature, leading to the sample deformation. Considering the size of these defects, they are mostly visible on the surface of the elements; however, in the case of more complex structures, the detection may be difficult. The wide application of AM elements and the possibility of the occurrence of the types of defects described above, make it necessary to develop diagnostic algorithms based on non-destructive testing (NDT).

One of the most powerful groups of NDT methods consists of techniques based on elastic wave propagation. Ultrasonic waves are a kind of high-frequency elastic waves capable of detection and imaging of structural damage. Thanks to their sensitivity to structural and material discontinuities of the medium, they already have been used by many researchers for diagnostics of various elements, e.g., concrete structures [13–15], composites [16–21] or adhesive joints [22–27]. A number of processing techniques were developed including weighted root mean square (WRMS) [16,17,20,22,26,28] or wavefield curvature imaging (WCI) [20]. A certain number of works were also performed on 3D-printed elements. A broad review of the application of ultrasonic waves for the diagnostics of AM elements manufactured from different filaments was presented by Honarvar and Varvani-Farahani [29]. The topic of damage identification in 3D-printed structures was considered by Acevedo et al. [30]. In their work, the use of elastic waves was proposed for the evaluation of residual stresses during sample production. The study on damage imaging in AM elements was performed by Na and Oneida [31], who visualized various defects (openings, inappropriate specimen manufacturing) in plates produced from ULTEM filament using a pulse-echo method. Another example of the successful application of ultrasonic waves for the diagnostics of AM elements was presented by Wang et al. [32], who proposed the use of phased array transducers for the detection of holes in titanium blocks. The defects with different sizes and locations were successfully identified and imaged.

Summarizing the mentioned works, there are no studies considering the application of guided wave propagation techniques in AM structures. Significantly, the samples made of commodity polymers (including PLA) have not been investigated. The aim of the current paper is to investigate the possibility of damage detection and imaging in AM plates made of PLA filament. Two samples were manufactured with defects in the form of reduced filling in certain parts of their volume. Guided waves were excited and recorded at the top surface of the plates using scanning laser Doppler vibrometry. The collected signals were processed using WRMS and WCI algorithms to reveal the location and shape of defects. Discussion of the results allowed stating that guided waves can be used for non-destructive testing of AM elements and characterizing the limitations of the used algorithms.

2. Materials and methods

2.1. Object of research

The research was conducted on two plate specimens produced with an additive manufacturing technique using PLA filament (figure 1). Both samples had dimensions of $100 \times 180 \times 3$ mm^3 and were printed in flat orientation with two different raster angles (alternately, 45º and –45º in consecutive layers). The samples had structural defects in the form of mesh with voids, i.e., reduced filling of material (from full void to dense mesh). In the first sample (#1) the defects were visible at one side of the plate and covered the two third of its thickness. In the second sample (#2) internal damages were introduced covering one-third of the plate thickness.

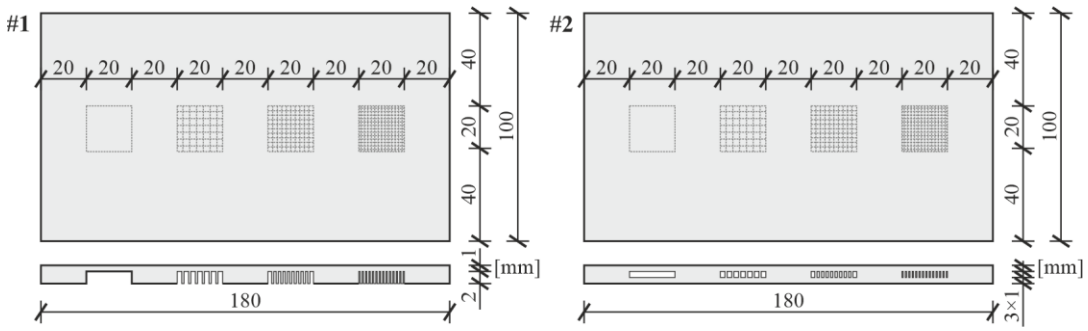

Figure 1. Object of research – geometry of plate samples made of PLA filament in top view and side view.

2.2. Experimental set-up and procedure

The samples were tested using scanning laser Doppler vibrometry (SLDV) based on the guided wave propagation technique. The experimental set-up is presented in figure 2a. The input signals of elastic waves were produced by the arbitrary function generator AFG 3022 (Tektronix, Inc.) and amplified with the high-voltage amplifier PPA 2000 (EC Electronics). The excitation had the form of a wave packet modulated from five cycles of sine function with different carrier frequencies (100 kHz, 200 kHz and 300 kHz for sample #1 and 100 kHz and 200 kHz for sample #2). The waves were excited with the use of the plate piezoelectric actuator NAC2024 (Noliac) which had dimensions of $3 \times 3 \times 2$ mm^3. The transducer was attached to each of the tested specimens by petro wax 080A109 (PCB Piezotronics, Inc.). The top surface of each tested sample was covered with retro-reflective sheeting to enhance the backscatter of light. The signals of propagating waves (velocity component perpendicular to plate surface) were recorded contactless in the number of points using the laser vibrometer PSV-3D-400-M (Polytec GmbH) equipped with a VD-07 velocity decoder. The measurement points (figure 2b) were organized in a regular mesh with 47 rows and 87 columns (4089 points in total), covering an area of 172×92 mm^2 (resulting in a scan resolution of 2 mm in both directions).

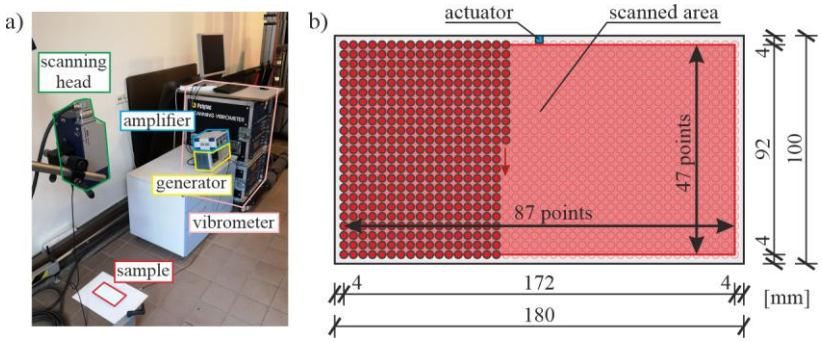

Figure 2. Experimental investigations: a) view of the test set-up, b) view of the measurement grid.

2.3. Damage imaging based on guided wave measurements

Since a guided wavefield (view of the wave signals in the tested area at a specific time instance) is mostly not efficient for damage imaging, additional signal processing is required to reveal the internal structure of the samples. It is a commonly known fact that wave propagation is strongly dependent on the homogeneity of the medium. Any discontinuities (boundaries, e.g., voids, cracks, or change of mechanical parameters) lead to disturbances in wave signals that can be barely observable in a guided wavefield but they have the potential to be detected and visualized with energy distribution-based techniques. In the current study, two methods were used.

2.3.1. Weighted root mean square technique. The first one is a simple but effective technique based on the calculation of a weighted root mean square (WRMS) calculation [16,20,22,26,28]. The WRMS value for a certain discrete time-domain signal $s_k = s(t_k)$ with a duration (time of averaging, time window) $t_e = (n-1)\Delta t$, containing n samples ($k = 1,2,\ldots,n$) spaced with a constant time interval Δt, can be calculated with respect to the formula:

$$WRMS = \left(\sum_{k=1}^{n} w_k s_k^2 \right)^{1/2} \tag{1}$$

where w_k denotes the so-called weighting factor that allows differentiating the influence of specific parts of the signal due to the time of propagation. In the literature [16,22,26,28] one can find several applications of the WRMS technique with a weighting factor in the following exponential form:

$$w_k = k^r \tag{2}$$

where r is a non-negative real value. In the classical approach $r = 0$, thus no averaging is introduced. It was proven by many studies [16,22,26,28] that satisfying results can be obtained for higher values of r, specifically $r = 1$ (linear weighting factor) and $r = 2$ (quadratic weighting factor).

2.3.2. Wavefield curvature imaging. The second method is wavefield curvature imaging (WCI) [20]. Assume that guided wavefield $w_{i,j,k}$ is represented discretely by a series of signals $s_k = s(t_k)$ recorded at a number of points organized in a regular mesh with p rows and q columns ($i = 1,2,\ldots,p$, $j = 1,2,\ldots,q$), while grid spacings between rows and columns are h_p and h_q, respectively. The first step in the WCI algorithm is the determination of wavefield energy function at each specific k-th time instance as:

$$E_k = \sum_{i=1}^{p} \sum_{j=1}^{q} w_{i,j,k}^2 \tag{3}$$

The function is then normalized to unity according to a maximum value corresponding to a specific sample k_m:

$$E_{n,k} = \frac{E_k}{E_{k_m}}, \qquad E_{k_m} = \max(E_k) \tag{4}$$

To minimize the effect of energy dissipation a so-called compensation function is introduced:

$$C_k = \begin{cases} 1 & \text{for } k < k_m \\ E_{n,k} & \text{for } k \geq k_m \end{cases} \tag{5}$$

According to the above-described compensation function, the compensated wavefield can be calculated as:

$$\tilde{w}_{i,j,k} = \frac{w_{i,j,k}}{C_k} \tag{6}$$

The next step is the wavefield curvature calculation as a central difference of the compensated wavefield:

$$z_{i,j,k} = \frac{\tilde{w}_{i+1,j,k} - 2\tilde{w}_{i,j,k} + \tilde{w}_{i-1,j,k}}{h_p^2} + \frac{\tilde{w}_{i,j+1,k} - 2\tilde{w}_{i,j,k} + \tilde{w}_{i,j-1,k}}{h_q^2} \tag{7}$$

The final step is energy fusion for a selected time window $[k_a, k_b]$ allowing to obtain the final energy map:

$$E_{F,i,j} = \sum_{k=k_a}^{k_b} z_{i,j,k}^2 \tag{8}$$

As a starting point of the time window, the moment of maximum energy can be used, thus $k_a = k_m$. In the current study, the use of the square root of the above-described energy function is proposed.

3. Results and discussion

3.1. WRMS damage maps

First, the results for the WRMS algorithm are presented. For both specimens some values of averaging time were tested, i.e., t_e = {0.1;0.25;0.5;1.0} ms (start point of time window was set as 0 ms). Three variants of weighting factors were considered: no averaging (r = 0) such as linear (r = 1) and quadratic (r = 2) weighting factors. The WRMS maps for sample #1 are presented in figures 3-5.

Figure 3 shows the results for excitation frequency 100 kHz. It can be seen that for the shortest averaging time (0.1 ms) the defects are barely visible for all weighting factors. The location of the excitation point is visible since the wave did not have enough time to propagate through the area of damage and the influence of the direct wave is significant. When no averaging is introduced, the influence of the first wave packet is crucial, regardless of the averaging time. For linear and quadratic weighting factors the shape of damage becomes much more pronounced with the increasing averaging time. The quality of maps is higher for 0.25 ms and 0.5 ms. Further increase of t_e does not make substantial change, because further parts of signals include significant noise. It is important to note that the first damaged area (total lack of material) is the most clearly visible because it is the most significant change in the structure. The two following areas (fine-meshed squares) are also imaged properly but with slightly lesser quality. The last defect (with the densest mesh) is not visible because the voids are very small and with the assumed measurement mesh with a 2 mm grid they are undetectable. It can be concluded that the appropriate results are obtained for linear and quadratic weighting factors for averaging time between 0.5 ms and 1.0 ms (these maps have similar and relatively good quality).

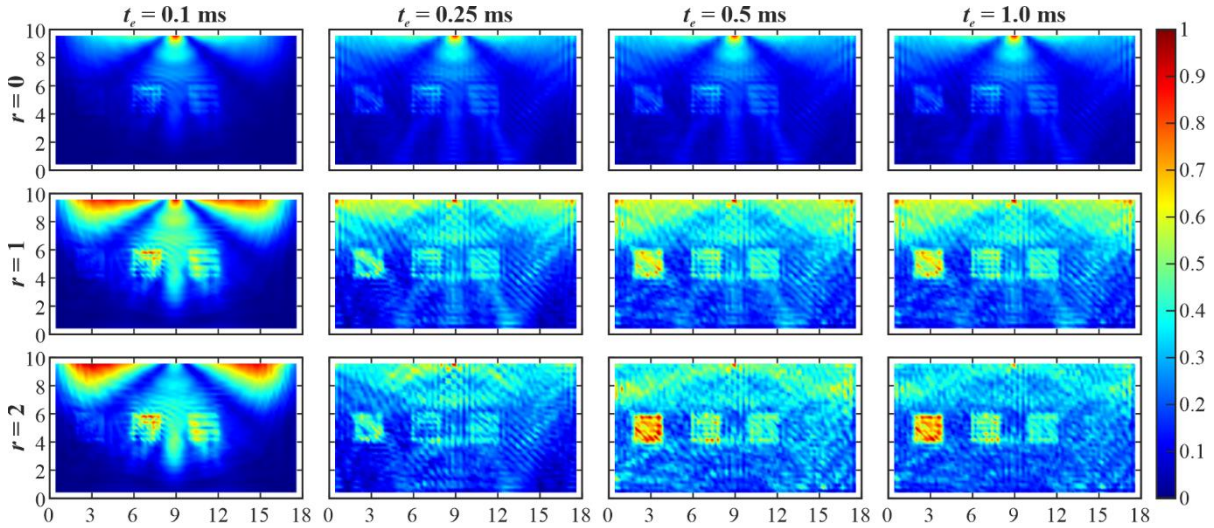

Figure 3. WRMS maps for specimen #1 (excitation frequency 100 kHz) for different weighting factors (rows) and averaging times (columns).

Similar conclusions can be drawn from the analysis of the results for excitation frequency equal 200 kHz (figure 4). However, it has to be noted that the quality of the maps is lower, in general. This is the effect of the use of higher-frequency waves that have significantly higher signal attenuation. This is specifically visible for the quadratic weighting factor and the longest averaging time, where no damage is imaged. This is the result of the fact, that the use of quadratic weighting factor significantly reduces the influence of the initial part of the signal (containing significant information) and increases the impact of the further part containing noise (more importantly than in the case of linear weighting factor that differentiates the influence of both signal parts less distinctly). This effect shows that higher excitation frequencies are less effective in damage imaging with WRMS in AM elements. On the other hand, since higher frequencies are related to the higher image resolution (due to the shorter

wavelength), the shape of the meshed defects is more accurately visualized. To sum up, a useful damage image is obtained for quadratic weighting factor and averaging time equal 0.5 ms.

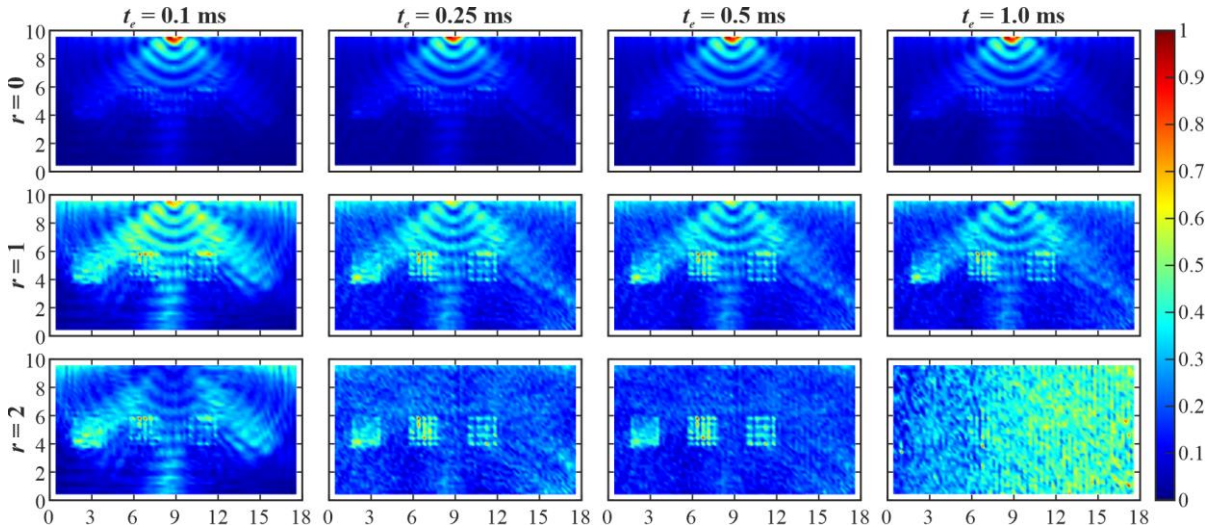

Figure 4. WRMS maps for specimen #1 (excitation frequency 200 kHz) for different weighting factors (rows) and averaging times (columns).

An important observation can be made based on the analysis of the results for sample #1 tested with an excitation frequency equal 300 kHz (figure 5). Due to the high attenuation of the wave signal the damaged areas are actually undetectable, regardless of the value of averaging time and weighting factor. The attenuation of wave amplitude is so high that the wave cannot propagate through the whole specimen before it vanishes. Only the influence of the direct signal in the vicinity of the excitation point is pronounced. If no averaging is introduced, the maps look almost the same for all averaging times. The use of linear and quadratic weighting factors barely changes the legibility of maps, however a slight image of the first defect (total void) can be observed for linear weighting factor (t_e equal 0.25 ms, 0.5 ms and 1.0 ms) and quadratic weighting factor (t_e equal 0.25 ms and 0.5 ms, for 1.0 ms the reduction of the initial part of the signal is too significant, similarly to the observations for 200 kHz). To sum up, it can be stated that an excitation frequency equal to 300 kHz is ineffective in damage imaging and based on this fact, it was not considered in the tests of specimen #2.

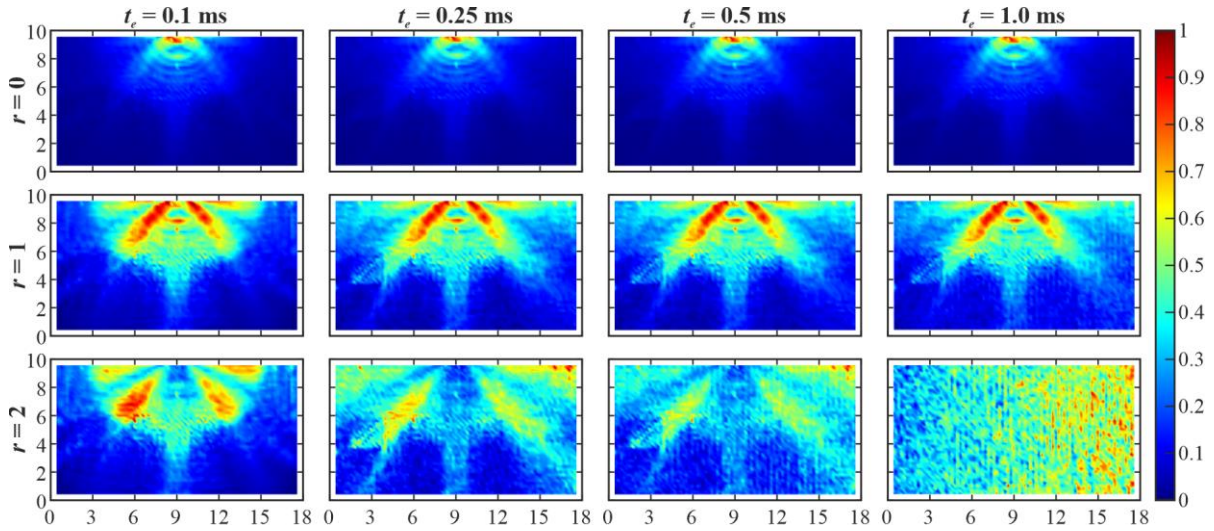

Figure 5. WRMS maps for specimen #1 (excitation frequency 300 kHz) for different weighting factors (rows) and averaging times (columns).

The results for specimen #2 for excitation frequency equal 100 kHz are presented in figure 6. Because the geometry of defects is similar in both samples #1 and #2, WRMS damage maps are also similar (cf. figure 3 and 6). The observations are the same with two exceptions. First, the defects are slightly less pronounced for sample #2, especially for longer averaging times. It is the result of the fact that in plate #2 the defects are internal and have a lower volume than in plate #1. Secondly, some unintended defect is observed in the lower part of the map for quadratic weighting factor and averaging time equal to 1.0 ms. It can be the result of weak bonding of retro-reflective sheeting in this part of the sample. The wave amplitude increases in this area after some time of propagation which explains the fact that it is visible only for the longest averaging time. In conclusion, the best quality of WRMS damage maps is observed for averaging time equal to 0.5 ms (linear and quadratic weighting factors) and 1.0 ms (only for linear variant).

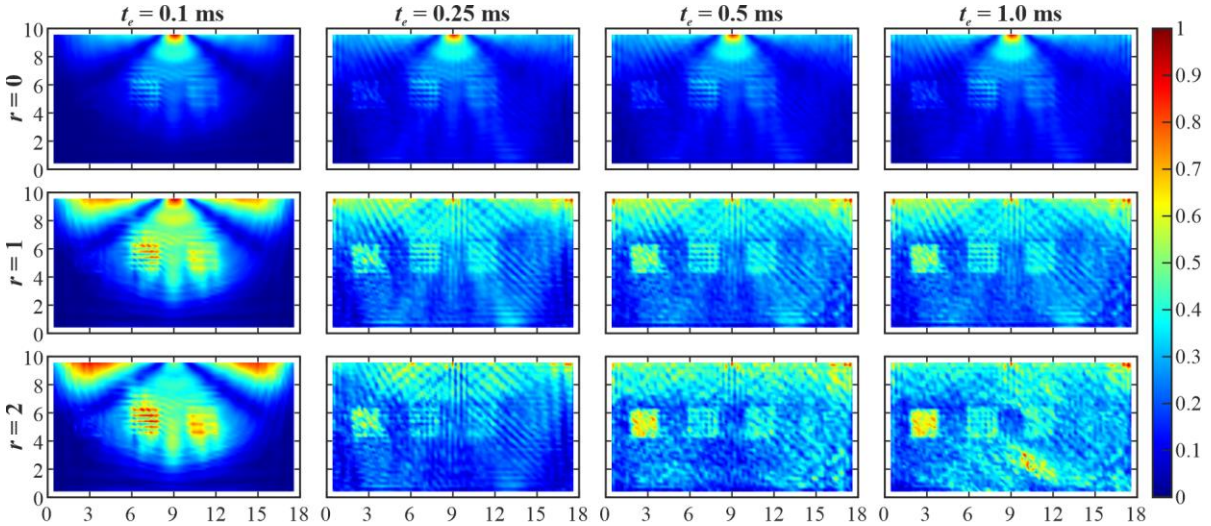

Figure 6. WRMS maps for specimen #2 (excitation frequency 100 kHz) for different weighting factors (rows) and averaging times (columns).

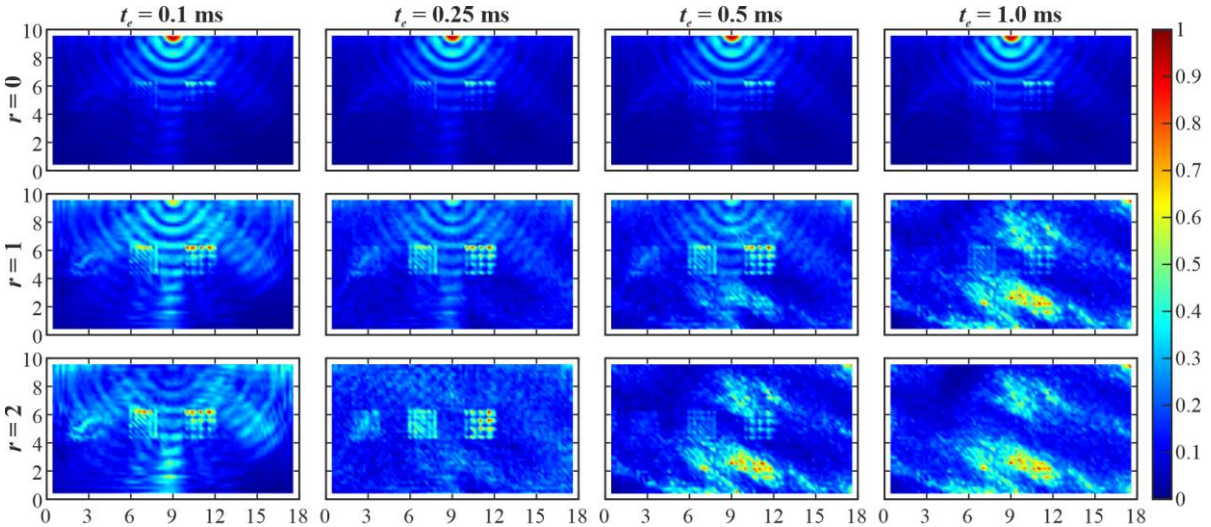

Figure 7. WRMS maps for specimen #2 (excitation frequency 200 kHz) for different weighting factors (rows) and averaging times (columns).

The visibility of the unintended defect in plate #2 is more pronounced for excitation frequency equal to 200 kHz (figure 7). It can be detected for linear and quadratic weighting factors for averaging time equal 0.5 ms and 1.0 ms. This is due to the higher attenuation of wave amplitude and shortening

of the useful part of signals. Similarly to sample #1, it can be stated that higher frequency improves the resolution of damage imaging (mesh defects are clearer), however, the influence of higher attenuation decreases the quality of maps significantly, compared to the results for 100 kHz (cf. figure 6 and 7). Even the most significant defect (full void, without meshing) is not clearly visible. The difference between the results for samples #1 and #2 for frequency 200 kHz (cf. figures 4 and 7) is significant, proving that the size of the defect strongly influences the possibility of its detection and imaging. Since the quality of WRMS damage maps for 200 kHz for sample #2 is poor, higher frequencies were not considered.

To sum up, damage imaging with the WRMS method strongly depends on the calculation parameters, such as the excitation frequency. It is crucial to choose the appropriate frequency and further, to analyze deeply different averaging times and variants of the weighting factor.

3.2. WCI damage maps

The results of damage imaging with the WCI method were prepared for the same data as WRMS maps. In contrast with the WRMS algorithm, which needs two parameters to be considered, WCI-based signal processing depends on the single parameter being time window length. To compare the results with both methods, the same end times of the time window were tested, i.e., $t_e = \{0.1;0.25;0.5;1.0\}$ ms. The start points were assumed to be time instances for which wavefield energy function reached the maximum, i.e., for sample #1: $t_s = 0.072$ ms (100 kHz), $t_s = 0.020$ ms (200 kHz), $t_s = 0.027$ ms (300 kHz) and for sample #2: $t_s = 0.070$ ms (100 kHz), $t_s = 0.021$ ms (200 kHz). As suggested in Section 2.3.2, the square root of the final energy function was used to prepare damage maps. The final values were normalized to unity.

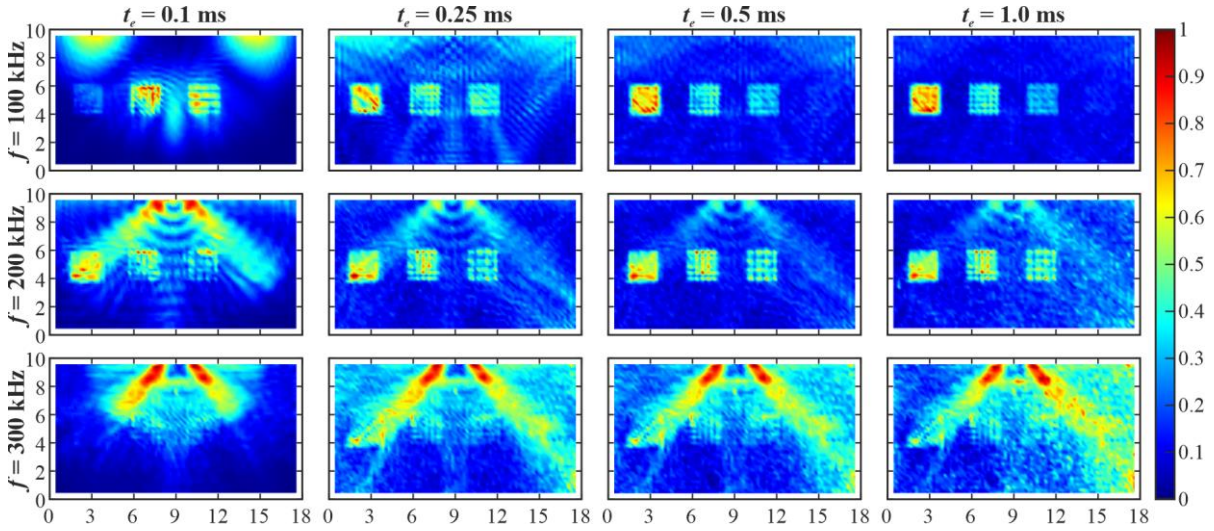

Figure 8. WCI maps for specimen #1 for different excitation frequencies (rows) and end times of time window (columns).

The results for specimen #1 are presented in figure 8. It can be clearly seen that the shortest time window (ending at t_e = 0.1 ms) gives a relatively low quality of damage images, regardless of excitation frequency. This is because the wave was not able to propagate appropriately through the damaged area and the influence of direct signal is significant. With the increasing time window length the shape of defects becomes more vivid. For excitation frequencies equal to 100 kHz and 200 kHz, the results for the following time windows have comparable quality. Similarly to the results obtained from the WRMS technique, the shape of the mesh is more pronounced for 200 kHz. In the case of frequency 300 kHz the strong attenuation makes damage imaging problematic. However, the shape of the defects can be partially identified for longer time windows (other than ending at 0.1 ms), and the quality of these images is better than all maps obtained using the WRMS technique. This shows an

advantage of WCI compared to WRMS. Final conclusion is that the best results (with comparable quality) are obtained for lower frequencies (100 kHz, 200 kHz), especially for longer time windows (ending at 0.25 ms, 0.5 ms and 1.0 ms).

Similar conclusions can be drawn from the analysis of the WCI results for sample #2 (figure 9). The image of defects for both frequencies is less pronounced than in sample #1 due to the different sizes of defects (like it was in WRMS results). The shortest time window seems to give poor-quality maps, but longer time windows show better visualizations. It can be noted, however, that for the longest time windows (ending at 1.0 ms for 100 kHz and at 0.5 ms and 1.0 ms for 200 kHz) the results reveal an unintended defect in the lower part of the sample (similar results were shown in WRMS maps). Thus, it can be stated that the best results can be obtained for the time window ending at 0.25 ms (both frequencies) and at 0.5 ms (100 kHz). In general, the damage maps obtained with WCI have much better quality than the ones obtained with WRMS.

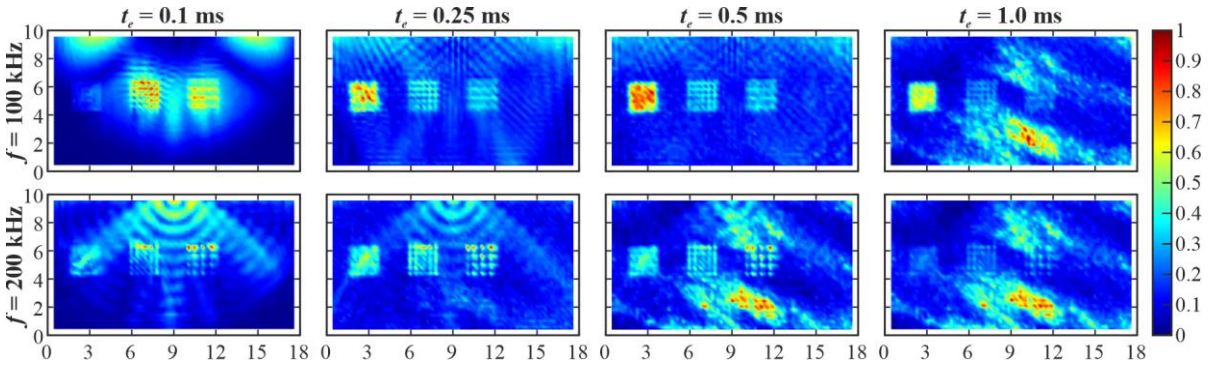

Figure 9. WCI maps for specimen #2 for different excitation frequencies (rows) and end times of time window (columns).

4. Conclusions

The paper dealt with the issue of damage imaging in 3D printed plate samples with defects in the form of voids with different geometry using ultrasonic guided wave measurements. Two promising techniques were considered, namely WRMS and WCI. Discussion of the results obtained allowed the following conclusions to be drawn.

The ultrasonic guided wave-based diagnostic methods can be successfully used for damage imaging in samples produced with the additive manufacturing method. There are, however, some important limitations of these methods.

Ultrasonic waves propagating in PLA experience strong attenuation, especially for higher excitation frequencies. This effect needs to be considered while testing samples with significant sizes. On the other hand, increasing the excitation frequency reduces the wavelength and increases the resolution of the damage image, allowing smaller defects to be seen in detail. It is important to appropriately choose the excitation frequency to minimize the strong attenuation effect and, simultaneously, maximize the accuracy of imaging.

The WCI algorithm has significant advantages compared to the WRMS algorithm. First, the WRMS method requires establishing two factors – averaging time and weighting scheme. Thus, to obtain effective results, a two-dimensional problem has to be solved. In the case of the WCI algorithm, only a time window has to be determined. Nevertheless, the results with WCI have better quality despite the parameters chosen.

The issue of guided wave-based damage imaging in 3D printed elements needs to be studied more deeply. Further works will focus on the development of algorithms for imaging different types of defects in this kind of elements, supported by finite element method calculations.

Acknowledgements

This research was funded by National Science Centre, Poland, 2021/41/N/ST8/01348.

References

[1] Jeong Y G Lee W S and Lee K B 2018 *J. Adv. Prosthodont.* **10** 245–51
[2] Javaid M and Haleem A 2019 *J. Oral Biol. Craniofacial Res.* **9** 179–85
[3] Yousef H Harris B T Elathamna E N Morton D and Lin W S 2021 *J. Prosthet. Dent.* 1–6
[4] Acharya A Chodankar R N Patil R and Patil A G 2023 *J. Oral Biol. Craniofacial Res.* **13** 253–8
[5] Haleem A Javaid M Khan R H and Suman R 2020 *J. Clin. Orthop. Trauma* **11** S118–24
[6] Roque R Barbosa G F and Guastaldi A C 2021 *J. Manuf. Process.* **64** 655–63
[7] Deering J and Grandfield K 2021 *Biomater. Biosyst.* **2** 100013
[8] Charbonnier B Hadida M and Marchat D 2021 *Acta Biomater.* **121** 1–28
[9] Meng M Wang J Sun T Zhang W Zhang J Shu L and Li Z 2022 *J. Orthop. Transl.* **34** 22–41
[10] Zhai W Ko Y Zhu W Wong A and Park C B 2009 *Int. J. Mol. Sci.* **10** 5381–97
[11] Castro-Aguirre E Iñiguez-Franco F Samsudin H Fang X and Auras R 2016 *Adv. Drug Deliv. Rev.* **107** 333–66
[12] Andrzejewska A 2018 *Adv. Intell. Syst. Comput.* **623** 399–408
[13] Rucka M and Wilde K 2013 *J. Nondestruct. Eval.* **32** 372–83
[14] Moradi-Marani F Rivard P Lamarche C P and Kodjo S A 2014 *Constr. Build. Mater.* **73** 663–73
[15] Rucka M and Wilde K 2015 *Bull. Polish Acad. Sci. Tech. Sci.* **63** 65–75
[16] Żak A Radzieński M Krawczuk M and Ostachowicz W 2012 *Smart Mater. Struct.* **21** 35024
[17] Hosseini S M H Duczek S and Gabbert U 2013 *Compos. Part B Eng.* **54** 1–10
[18] Zhang X Wu X He Y Yang S Chen S Zhang S and Zhou D 2019 *Compos. Part B Eng.* **168** 152–8
[19] Sikdar S Van Paepegem W Ostachowicz W and Kersemans M 2020 *Compos. Part B Eng.* **200** 108304
[20] Sha G Xu H Radzieński M Cao M Ostachowicz W and Su Z 2021 *Mech. Syst. Signal Process.* **150** 107240
[21] Wandowski T Radzienski M Mindykowski D and Kudela P 2023 *Ultrasonics* **(in press)** 106986
[22] Rucka M Wojtczak E and Lachowicz J 2018 *Appl. Sci.* **8** 1–9
[23] Sha G Radzienski M Soman R Wandowski T Cao M and Ostachowicz W 2020 *Smart Mater. Struct.* **30** 15001
[24] Castaings M Hosten B and François D 2004 *Ultrasonics* **42** 1067–71
[25] Spytek J Ziaja-Sujdak A Dziedziech K Pieczonka L Pelivanov I and Ambrozinski L 2020 *NDT E Int.* **112** 102249
[26] Marks R Clarke A Featherston C Paget C and Pullin R 2016 *Appl. Sci.* **6** 12
[27] Wojtczak E and Rucka M 2022 *Compos. Struct.* **297** 115930
[28] Wojtczak E Rucka M and Knak M 2020 *Materials (Basel).* **13** 1–19
[29] Honarvar F and Varvani-Farahani A 2020 *Ultrasonics* **108** 106227
[30] Acevedo R Sedlak P Kolman R and Fredel M 2020 *J. Mater. Res. Technol.* **9** 9457–77
[31] Na J K and Oneida E K 2018 *Addit. Manuf.* **24** 154–65
[32] Wang X Li W Li Y Zhou Z Zhang J Zhu F and Miao Z 2020 *Mater. Res. Express* **7** 16572